MNRAS 000, 1–15 (0000) Preprint 28 August 2023 Compiled using MNRAS LATEX style file v3.0

Synthetic gravitational lens image of the Sgr A* black hole with a thin disk model

Ezequiel F. Boero,[1]★ and Osvaldo M. Moreschi,[2,3]†
[1] Instituto de Astronomía Teórica y Experimental (IATE), CONICET,
Observatorio Astronómico de Córdoba,
Laprida 854, (X5000BGR) Córdoba, Argentina.
[2]Facultad de Matemática, Astronomía, Física y Computación (FaMAF),
Universidad Nacional de Córdoba,
[3]Instituto de Física Enrique Gaviola, IFEG, CONICET,
Ciudad Universitaria, (5000) Córdoba, Argentina.

Accepted XXX. Received YYY; in original form ZZZ

ABSTRACT
The images of Sagittarius A* produced by the Event Horizon Telescope (ETH) Collaboration in 2022 present features that were associated with a emission ring consistent with what is expected from an accretion disc surrounding the supermassive black hole at the center of our Galaxy. We study different configurations of a simple accretion disc model that became successful in reproducing the main features observed in M87* together with a ray tracing-technique that accounts for magnification effects along null geodesic bundles. In particular, we explore in detail the case of nearly edge-on configurations which are a priori the most expected configurations for a relaxed disc. Our results show that these scenarios remain viable when compared with images reconstructed with data from April 6 and 7 of 2017.

Key words: gravitational lensing: strong – gravitation – black hole physics

1 INTRODUCTION

The immediate surroundings of supermassive black holes (SMBH) in scales of a few Schwarzschild radius were resolved for the first time in recent years Akiyama et al. (2019a, 2022a). Utilizing the Very Long Baseline Interferometry (VLBI) facilities, comprised in the Event Horizon Telescope (EHT), the first images corresponding to M87* at the center of the nearby elliptical galaxy M87(Akiyama et al. 2019b) and Sagittarius A*(Akiyama et al. 2022c), the SMBH hosted in our Galaxy were obtained. These observations were carried in the millimiter radio wave band attaining a resolution through the several campaigns of approximately $\sim 20\mu$arcseconds. Most of the reconstructed images using different methods often reveal a prominent ring-like structure, which corresponds to the emission from hot gas around the event horizon of the black holes. Comparison with a bank template of GRMHD numerical simulations indicates that indeed the geometry of the central object is compatible with a Kerr black hole. However, due to the intrinsic limitations in the imaging process, the interpretation of the diverse features of the images is not completely clear due to the degeneracy in the models that could explain it.

We have studied in the past the case of M87* Boero & Moreschi (2021) assuming a simple scenario for the emission in terms a disc region having two temperatures as commonly observed in GRMHD simulations and we obtained images with a new approach that combines the integration of geodesics and geodesic deviation equation in an very efficient way Boero & Moreschi (2020). As a result we found that our images could fit very well reported final images of the EHT Collaboration.

In this article we focus on the most recent EHT publications on Sagittarius A*Akiyama et al. (2022a,b,c,d,e,f); we carry a similar analysis to our previous work, motivated by the good results we had obtained; and noting that both SMBH have almost the same angular size.

Both systems are catalogued as low luminosity AGNs (LLAGNs) and characterized by accretion rates satisfying $\dot{M} \ll \dot{M}_{\rm crit}$ with $c^2\dot{M}_{\rm crit} = \dot{L}_{\rm Edd}$; The Eddington's luminosity limit $L_{\rm Edd}$ becomes a useful parameter that determines in most accretion model the characteristic of the disc and its emission properties. For the case of M87* and Sgr A* the discs is expected to present properties consistent with emission coming from an optically thin disc where very hot flows are accreted mainly through advection processes (Shapiro et al. 1976; Ichimaru 1977; Narayan & Yi 1994; Abramowicz

★ E-mail: ezequiel.boero@unc.edu.ar
† E-mail: o.moreschi@unc.edu.ar

terial in the vicinity of the BH is an ionized plasma with electrons and ions having different temperatures.

The EHT Collaboration has provided a physical scenario for the geometry and the accretion flow orbiting Sgr A* based on comparison of the data with several synthetic images from diverse models. From their analysis they claim that the orbiting plasma is most probably described by magnetically arrested disc (MAD) which tend to be strongly magnetized.

As in their previous work on M87, the EHT team emphasizes that the images could be mainly understood in terms of a ring structure; however we have also shown in our article on the same system, that the images might as well be understood in terms of the natural structure of a disk model. What is somehow striking in the described construction process used by EHT Coolaboration in the Sgr A*(Akiyama et al. 2022c) case is the fact, see for example their figures 7, 11 and 12, that the models involving rings, crescents, disks and other general relativistic magnetohydrodynamic (GRMHD) calculations, are almost face-on configurations. Since as observers we are situated more or less in the equatorial plane of the galaxy, it would be natural to assume first a ring or disk structure that it would be close to its plane of symmetry, that is, one would expect to have an edge-on view. We tackle this issue in this article.

As it was the case of the previous works of EHT(Akiyama et al. 2019a), the spectral energy distribution of such systems presents features that are thought to be associated with emission from an *optically thin and geometrically thick accretion disk* with an observed brightness temperature in radio wavelengths in the range of $10^9 - 10^{10}$K. The expectation, as it was the case of M87, the emission collected at sub-millimeter wavelength of ($\sim$ 230GHz) is thought to be weakly absorbed by the surrounding media, allowing to detect the immediate vicinity of the event horizon of the associated SMBH.

Whenever possible, for tensors and vectors objects, we will employ standard abstract index notation with Latin letters $a, b, c, ...$ for tensor fields. Our choice of signature for the spacetime metric g_{ab} is $(+, -, -, -)$.

One of the main characteristics of the observation of Sgr A* is its time variability. In turn, this complicates considerably the reconstruction of an image from the observed data. For this reason as mentioned in (Akiyama et al. 2022c,d) the EHT team must rely on different kind of models. In fact, their methodology for the construction of images is to use a variety of models for the matter distribution around the supermassive black hole. Due to the unexpected geometry suggested for the EHT image, here shown in Fig. 1, we study first a thin accretion disk whose plane is inclined with respect of the plane of the galaxy, us suggested by the EHT image. We have considered a big range for the projected angular momentum of the black hole with the line of sight, and also a range of values for the possible total angular momentum of the black hole. Since we were not convinced with the results of this study, that we present below, we have also considered the more natural assumption of an accretion disk and black hole angular momentum that have small angles with respect to the plane of the galaxy and angular momentum of the galaxy respectively. In our opinion, this last model gives better results than the previous one.

The organization of the article is as follows. In the next second section we review the basic equations that we use in our construction. Since they were discussed at length in our previous article (Boero & Moreschi 2021) we present here a shorter summary of the basic dynamical equations for the deviation vector and the optical scalars equations. In section 3 we describe the geometry, the evolution equations, the conserved quantities, the initial conditions and details of the matter model. Our image constructions are presented in section 4. We take the opportunity in this case to also present the calculation of the expected silhouette of the black hole for different configurations in section 5. We reserve the final section 6 for some recapitulation and comments; where we argue that our resulting image is very closely related to the April 6 image coming from the their Themis pipeline.

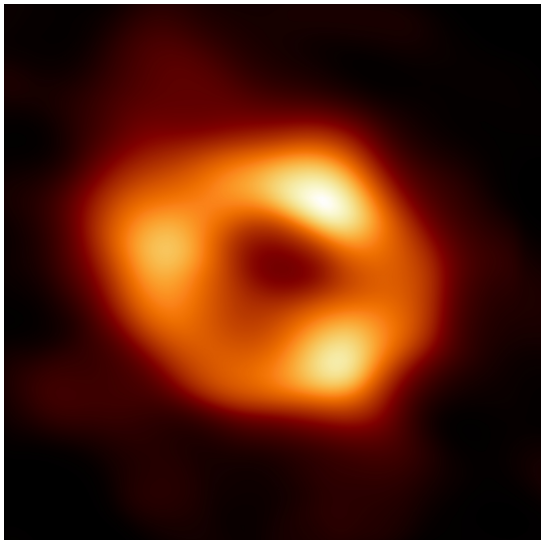

Figure 1. Image from the EHT Collaboration of Sagittarius A*; where they show an average of reconstructed images for April 7.

2 EXACT GRAVITATIONAL LENS OPTICAL SCALARS

2.1 The basic equations

Although we have discussed the notion of 'exact gravitational lens optical scalars' in the past(Boero & Moreschi 2021), we here introduce an alternative for the initial conditions, improve the notation and correct a typo of the last version.

The general setting is to consider the null geodesics in the past null cone of an observer moving with 4-velocity v^a. The tangent vectors to the null geodesics are denoted by ℓ^a, which are past directed; so that are normalized by the condition:

$$\ell^a v_a = -1, \tag{1}$$

and since they are null geodesics, we also have

$$\ell^a \nabla_a \ell^b = 0, \tag{2}$$

where ∇_a is the covariant derivative in terms of abstract indices.

In order to calculate the optical scalars we need to introduce the geodesic deviation vector η^a which

null tetrad $(\ell^a, m^a, \bar{m}^a, n^a)$ where m^a and $\bar{m}^a$ is a pair of complex conjugated vectors and n^a an additional real null vector. We choose the two complex vectors m^a and $\bar{m}^a$ to be parallel propagated along the geodesic. Then, we express the geodesic deviation vector as

$$\varsigma^a = \varsigma \bar{m}^a + \bar{\varsigma} m^a + \eta \ell^a. \tag{3}$$

Using that ς^a must be Lie transported along the null geodesics, one arrives at the geodesic deviation equations:

$$\ell^a \nabla_a \left(\ell^b \nabla_b \varsigma^d \right) = R_{abc}{}^d \ell^a \varsigma^b \ell^c; \tag{4}$$

where $R_{abc}{}^d$ denotes the Riemann tensor. Then the task is to solve the couple system of differential equations (2) and (4).

2.2 Optical scalars

Let us define here explicitly the exact gravitational optical scalars.

The situation we are considering is that of an observed deviation $\delta\theta^i$ from a reference observed direction in the sky, denoted by θ, corresponding to the direction of the null geodesic described by ℓ^a. In the absence of gravitational effects one would detect the deviation $\delta\beta^i$ with respect to the reference direction β. Then, the optical scalars κ, γ_1, γ_2 and ω are defined through the linear relation between $\delta\theta^i$ and $\delta\beta^i$

$$\delta\beta^i = \mathcal{A}^i{}_j \, \delta\theta^j, \tag{5}$$

were the matrix $\mathcal{A}^i{}_j$ is given by

$$\mathcal{A}^i{}_j = \begin{pmatrix} 1-\kappa-\gamma_1 & -\gamma_2-\omega \\ -\gamma_2+\omega & 1-\kappa+\gamma_1 \end{pmatrix}. \tag{6}$$

Let us note that the component ς is complex, and that their real and imaginary parts $(\varsigma_R, \varsigma_I)$, can be used as components in a real 2-dimensional plane; orthogonal to ℓ^a and therefore they will be related to the angles $\delta\theta^i$ and $\delta\beta^i$. We will denote with υ_R and υ_I the derivatives of ς_R and ς_I respectively, along the null geodesic ℓ^a. Then the initial conditions for the couple differential equation, that is at the observer position, are:

$$\delta\theta^i \equiv \begin{pmatrix} \upsilon_R \\ \upsilon_I \end{pmatrix}\Big|_{\lambda=0} \equiv \begin{pmatrix} \ell(\varsigma_R) \\ \ell(\varsigma_I) \end{pmatrix}\Big|_{\lambda=0}, \tag{7}$$

and

$$\varsigma^i\Big|_{\lambda=0} = \begin{pmatrix} \varsigma_R \\ \varsigma_I \end{pmatrix}\Big|_{\lambda=0} = \begin{pmatrix} 0 \\ 0 \end{pmatrix}; \tag{8}$$

where we are using λ to denote the affine parameter along the null geodesic.

At the target point the affine parameter has the value λ_s and then by definition one has

$$\delta\beta^i \equiv \frac{1}{\lambda_s} \begin{pmatrix} \varsigma_R \\ \varsigma_I \end{pmatrix}\Big|_{\lambda=\lambda_s}. \tag{9}$$

Let us note that ς has units of length. The unit of length might be relatively big or small with respect to the size of the system. Then, equations (5) and (6) explicitly become:

$$\frac{\varsigma_R}{\lambda_s} = (1-\kappa-\gamma_1)\upsilon_R - (\gamma_2+\omega)\upsilon_I, \tag{10}$$

$$\frac{\varsigma_I}{\lambda_s} = -(\gamma_2-\omega)\upsilon_R + (1-\kappa+\gamma_1)\upsilon_I. \tag{11}$$

In relation to the integration process of the geodesic deviation equation, it is probably worthwhile to mention that while on the right hand side of the above equations, the υ_R and υ_I are evaluated at the observer position, on the left hand side the ς_R and ς_I are evaluated at the source position. Since it is a 2-dimensional system we need to consider two independent initial conditions. Due to the fact that we are in the galaxy and that a possible disk around Sagittarius A* would probably sustain a very small angle, we have considered in the numerical calculation a couple of initial conditions; just to see if the computation was sensible to them.

The first standard choice for initial conditions is to take

$$\begin{pmatrix} \varsigma_{R_1} \\ \varsigma_{I_1} \end{pmatrix}\Big|_{\lambda=0} = \begin{pmatrix} 0 \\ 0 \end{pmatrix}, \tag{12}$$

$$\begin{pmatrix} \upsilon_{R_1} \\ \upsilon_{I_1} \end{pmatrix}\Big|_{\lambda=0} = \frac{1[\mathsf{L}]}{\lambda_s} \begin{pmatrix} 1 \\ 0 \end{pmatrix}, \tag{13}$$

and

$$\begin{pmatrix} \varsigma_{R_2} \\ \varsigma_{I_2} \end{pmatrix}\Big|_{\lambda=0} = \begin{pmatrix} 0 \\ 0 \end{pmatrix}, \tag{14}$$

$$\begin{pmatrix} \upsilon_{R_2} \\ \upsilon_{I_2} \end{pmatrix}\Big|_{\lambda=0} = \frac{1[\mathsf{L}]}{\lambda_s} \begin{pmatrix} 0 \\ 1 \end{pmatrix}, \tag{15}$$

where L is the unit of length (which it could be taken as λ_s) and which yields the final linear system of equations for the quantities κ, γ_1, γ_2 and ω:

$$\frac{\varsigma_{R1}}{[\mathsf{L}]} = (1-\kappa-\gamma_1), \tag{16}$$

$$\frac{\varsigma_{I1}}{[\mathsf{L}]} = -(\gamma_2-\omega), \tag{17}$$

$$\frac{\varsigma_{R2}}{[\mathsf{L}]} = -(\gamma_2+\omega), \tag{18}$$

$$\frac{\varsigma_{I2}}{[\mathsf{L}]} = (1-\kappa+\gamma_1), \tag{19}$$

or equivalently

$$\kappa = 1 - \frac{\varsigma_{R1}+\varsigma_{I2}}{2[\mathsf{L}]}, \tag{20}$$

$$\gamma_1 = \frac{\varsigma_{I2}-\varsigma_{R1}}{2[\mathsf{L}]}, \tag{21}$$

$$\gamma_2 = -\frac{\varsigma_{I1}+\varsigma_{R2}}{2[\mathsf{L}]}, \tag{22}$$

$$\omega = \frac{\varsigma_{I1}-\varsigma_{R2}}{2[\mathsf{L}]}. \tag{23}$$

It is worthwhile to mention that in a numerical work the choice of the unit of length $[\mathsf{L}]$ is an important detail to have in mind, since; although the geodesic deviation equation is linear, and therefore we would be free to use any magnitudes, from the numerical point of view, one does not want to have very different orders of magnitude for the couple system of ordinary differential equations. This is precisely adjusted with the choice of unit of length. It is for this reason that we have chosen now to introduce explicitly the choice of unit of length in the notation.

The second set of initial conditions we have considered is just a 45° rotated [illegible] namely, we have taken the

observer position:

$$\begin{pmatrix}\varsigma_{R_1}\\ \varsigma_{I_1}\end{pmatrix}\Big|_{\lambda=0}=\begin{pmatrix}0\\0\end{pmatrix}, \tag{24}$$

$$\begin{pmatrix}\upsilon_{R_1}\\ \upsilon_{I_1}\end{pmatrix}\Big|_{\lambda=0}=\frac{1[\mathsf{L}]}{\lambda_s}\begin{pmatrix}\frac{1}{\sqrt{2}}\\ \frac{1}{\sqrt{2}}\end{pmatrix}, \tag{25}$$

and

$$\begin{pmatrix}\varsigma_{R_2}\\ \varsigma_{I_2}\end{pmatrix}\Big|_{\lambda=0}=\begin{pmatrix}0\\0\end{pmatrix}, \tag{26}$$

$$\begin{pmatrix}\upsilon_{R_2}\\ \upsilon_{I_2}\end{pmatrix}\Big|_{\lambda=0}=\frac{1[\mathsf{L}]}{\lambda_s}\begin{pmatrix}-\frac{1}{\sqrt{2}}\\ \frac{1}{\sqrt{2}}\end{pmatrix}. \tag{27}$$

These equations yield the final linear system of equations for the quantities κ, γ_1, γ_2 and ω:

$$\frac{\varsigma_{R1}}{[\mathsf{L}]}=(1-\kappa-\gamma_1)\frac{1}{\sqrt{2}}-(\gamma_2+\omega)\frac{1}{\sqrt{2}}, \tag{28}$$

$$\frac{\varsigma_{I1}}{[\mathsf{L}]}=-(\gamma_2-\omega)\frac{1}{\sqrt{2}}+(1-\kappa+\gamma_1)\frac{1}{\sqrt{2}}. \tag{29}$$

$$\frac{\varsigma_{R2}}{[\mathsf{L}]}=-(1-\kappa-\gamma_1)\frac{1}{\sqrt{2}}-(\gamma_2+\omega)\frac{1}{\sqrt{2}}, \tag{30}$$

$$\frac{\varsigma_{I2}}{[\mathsf{L}]}=(\gamma_2-\omega)\frac{1}{\sqrt{2}}+(1-\kappa+\gamma_1)\frac{1}{\sqrt{2}}, \tag{31}$$

or equivalently

$$\kappa+\omega=1-\frac{\varsigma_{R1}+\varsigma_{I2}}{\sqrt{2}[\mathsf{L}]}, \tag{32}$$

$$\gamma_1+\gamma_2=\frac{\varsigma_{I2}-\varsigma_{R1}}{\sqrt{2}[\mathsf{L}]}, \tag{33}$$

$$-\gamma_1+\gamma_2=-\frac{\varsigma_{I1}+\varsigma_{R2}}{\sqrt{2}[\mathsf{L}]}, \tag{34}$$

$$-\kappa+\omega=-1+\frac{\varsigma_{I1}-\varsigma_{R2}}{\sqrt{2}[\mathsf{L}]}; \tag{35}$$

so that

$$\kappa=1+\frac{1}{2}\Big(-\frac{\varsigma_{R1}+\varsigma_{I2}}{\sqrt{2}[\mathsf{L}]}-\frac{\varsigma_{I1}-\varsigma_{R2}}{\sqrt{2}[\mathsf{L}]}\Big), \tag{36}$$

$$\gamma_1=\frac{1}{2}\Big(\frac{\varsigma_{I2}-\varsigma_{R1}}{\sqrt{2}[\mathsf{L}]}+\frac{\varsigma_{I1}+\varsigma_{R2}}{\sqrt{2}[\mathsf{L}]}\Big), \tag{37}$$

$$\gamma_2=\frac{1}{2}\Big(\frac{\varsigma_{I2}-\varsigma_{R1}}{\sqrt{2}[\mathsf{L}]}-\frac{\varsigma_{I1}+\varsigma_{R2}}{\sqrt{2}[\mathsf{L}]}\Big), \tag{38}$$

$$\omega=\frac{1}{2}\Big(\frac{\varsigma_{I1}-\varsigma_{R2}}{\sqrt{2}[\mathsf{L}]}-\frac{\varsigma_{R1}+\varsigma_{I2}}{\sqrt{2}[\mathsf{L}]}\Big). \tag{39}$$

It important to note that the calculation of the magnification factor μ, in terms of the final values of the deviation vector, is independent of the initial angle choice and is given by:

$$\mu=\frac{1}{(1-\kappa)^2-(\gamma_1^2+\gamma_2^2)+\omega^2}=\frac{[\mathsf{L}]}{\varsigma_{I2}\varsigma_{R1}-\varsigma_{I1}\varsigma_{R2}}. \tag{40}$$

3 RAY-TRACING EQUATIONS

3.1 Null geodesics and the null geodesic deviation equation in Kerr spacetime

In the simulation of the lensing effects of the material surrounding the immediate vicinity of Sagittarius A* we will assume as in Boero & Moreschi (2021) that the underling geometry is given by the two parametric (M,a) Kerr line element:

$$\begin{aligned}ds^2=&(1-\Phi)\,dt^2+2\Phi a\sin(\theta)^2dtd\phi-\frac{\Sigma}{\Delta}dr^2\\&-\Sigma d\theta^2-\big(r^2+a^2+\Phi a^2\sin^2(\theta)\big)\sin(\theta)^2d\phi^2.\end{aligned} \tag{41}$$

As usual M denotes the mass of the spacetime and a the rotation parameter respectively and the functions $\Sigma(r,\theta)$, $\Delta(r)$ and $\Phi(r,\theta)$ are given by

$$\Sigma=r^2+a^2\cos(\theta)^2, \tag{42}$$

$$\Delta=r^2-2rM+a^2, \tag{43}$$

$$\Phi=\frac{2Mr}{\Sigma}. \tag{44}$$

Beyond being quite ubiquitous to describe the expected gravitational field in the neighbourhood of the central core of a galaxy, Kerr metric has the nice feature that both geodesics and null geodesic deviation equations acquire expressions that permit a relatively easy treatment Carter (1966); Boero & Moreschi (2020).

For numerical purposes the full system of equations can be cast as a first order system as follows:

$$\dot{t}=\frac{1}{\Sigma\Delta}\Big[E\Big((r^2+a^2)^2-\Delta\,a^2\sin(\theta)^2\Big)-2aMrL_z\Big], \tag{45}$$

$$\dot{r}=v^r, \tag{46}$$

$$\begin{aligned}\dot{v^r}=&(v^\theta)^2r\frac{\Delta}{\Sigma}+\frac{a^2}{\Sigma}\dot{r}\dot{\theta}\sin(2\theta)-(v^r)^2\frac{r\Delta+(M-r)\,\Sigma}{\Sigma\Delta}\\&-\dot{t}^2\frac{M\Delta\big(r^2-a^2\cos(\theta)^2\big)}{\Sigma^3}\\&+2\dot{t}\dot{\phi}\frac{aM\Delta\big(r^2-a^2\cos(\theta)^2\big)\sin(\theta)^2}{\Sigma^3}\\&+\dot{\phi}^2\frac{\Delta\sin(\theta)^2}{\Sigma^3}\Big(r\Sigma^2\\&\qquad-a^2M\big(r^2-a^2\cos(\theta)^2\big)\sin(\theta)^2\Big),\end{aligned} \tag{47}$$

$$\dot{\theta}=v^\theta, \tag{48}$$

$$\begin{aligned}\dot{v^\theta}=&\frac{a^2Mr\sin(2\theta)}{\Sigma^3}\dot{t}^2-\frac{2aMr\left(r^2+a^2\right)\sin(2\theta)}{\Sigma^3}\dot{t}\dot{\phi}\\&-\frac{a^2\sin(2\theta)}{2\Sigma\Delta}(v^r)^2-\frac{2r}{\Sigma}\dot{r}\dot{\theta}+\frac{a^2\sin(2\theta)}{2\Sigma}(v^\theta)^2\\&+\frac{\sin(2\theta)}{2\Sigma^3}\Big(\left(r^2+a^2\right)\Sigma^2\\&\qquad+2a^2rM\sin(\theta)^2\left(r^2+a^2+\Sigma\right)\Big)\dot{\phi}^2,\end{aligned} \tag{49}$$

$$\dot{\phi}=\frac{1}{\Sigma\Delta}\left[2EaMr+(\Sigma-2Mr)\frac{L_z}{\sin(\theta)^2}\right], \tag{50}$$

$$\dot{\varsigma}_{R1}=\upsilon^{\varsigma}_{R1}, \tag{51}$$

$$\dot{\upsilon}^{\varsigma}_{R1}=-\varsigma_{R1}\Psi_{0R}-\varsigma_{I1}\Psi_{0I}, \tag{52}$$

$$\dot{\varsigma}_{I1}=\upsilon^{\varsigma}_{I1}, \tag{53}$$

$$\dot{\upsilon}^{\varsigma}_{I1}=-\varsigma_{R1}\Psi_{0I}+\varsigma_{I1}\Psi_{0R}, \tag{54}$$

$$\dot{\varsigma}_{R2} = \upsilon^{\varsigma}_{R2}, \tag{55}$$
$$\dot{\upsilon}^{\varsigma}_{R2} = -\varsigma_{R2}\Psi_{0R} - \varsigma_{I2}\Psi_{0I}, \tag{56}$$
$$\dot{\varsigma}_{I2} = \upsilon^{\varsigma}_{I2}, \tag{57}$$
$$\dot{\upsilon}^{\varsigma}_{I2} = -\varsigma_{R2}\Psi_{0I} + \varsigma_{I2}\Psi_{0R}. \tag{58}$$

In the above expressions, the constants of motion E and L along the central null geodesics are obtained through its relation to the coordinates (r_o, θ_o) of an stationary observer and the directions of the incoming photons (α_x, δ_z) through the following expressions:

$$E = -\sqrt{1-\Phi_o}, \tag{59}$$

$$\alpha_x = \frac{L_z}{r_o \sin(\theta_o)}, \tag{60}$$

$$\delta_z = -\frac{(\pm)}{r_o}\left[K - \left(\frac{L_z}{\sin(\theta_o)} - aE\sin(\theta_o)\right)^2\right]^{1/2}, \tag{61}$$

where K is Carter's constant. It should be noticed that in the numerical calculations we first choose α_x and δ_z, from which we infer, at the observer position, the values of the constant of motion L_z and K; although K does not appear in the evolution equations; but they both appear in the initial conditions. The Weyl curvature scalar $\Psi_0 = \Psi_{0R} + i\Psi_{0I}$ is given by the compact expression(Boero & Moreschi 2020):

$$\Psi_0 = -\frac{3M^{5/3}\mathbb{K}^2}{2\big(r - ia\cos(\theta)\big)^5}; \tag{62}$$

where the constant $\mathbb{K}$ is a spin-weight quantity given by:

$$\mathbb{K} = \frac{i\sqrt{2}}{M^{1/3}}\left[\delta_z r_o - i\big(-aE\sin(\theta_o) + \alpha_x r_o\big)\right], \tag{63}$$

and satisfies $\mathbb{K}\bar{\mathbb{K}} = 2M^{-2/3}K^2$.

The appropriated initial conditions for the geodesic equation are

$$t_0 = t_o = 0, \tag{64}$$
$$r_0 = r_o, \tag{65}$$
$$v^r_0 = -\frac{\sqrt{\mathcal{R}(r_o)}}{\Sigma_o}, \tag{66}$$
$$\theta_0 = \theta_o, \tag{67}$$
$$\ell^{\theta}_0 = \pm\frac{\sqrt{\Theta(\theta_o)}}{\Sigma_o}, \tag{68}$$
$$\phi_0 = \phi_o = -\frac{\pi}{2}, \tag{69}$$

where the functions $\mathcal{R}(r)$ and $\Theta(\theta)$ are defined as

$$\mathcal{R}(r) = \Big(E\left(r^2+a^2\right) - aL\Big)^2 - K\Delta(r), \tag{70}$$

$$\Theta(\theta) = K - \left(\frac{L}{\sin(\theta)} - aE\sin(\theta)\right)^2. \tag{71}$$

For the geodesics deviation equations one can use for example either of the choices previously described in the section 2, namely the set of initial conditions (12) - (15) or (24) - (27).

3.2 Simple accretion disc model in Kerr

Our working assumption is of a geometrically thin disk, where the matter motion is confined to the equatorial plane, with circular orbits; that is, we neglect the radial component of the velocity in this model. Assigning the label 'e' to an emitter, then its motion is characterized by the values of radial and angular coordinates $(r = r_e, \theta = \pi/2)$, and by its four velocity $u^a_e = \left(\dot{t}_e, 0, 0, \dot{\phi}_e\right)^a$; in such a way that we have the following equations of motion:

$$r_e^2\dot{t}_e = \frac{1}{\Delta_e}\left[E_e\Big((r_e^2+a^2)^2 - \Delta\, a^2\Big) - 2aMr_eL_e\right], \tag{72}$$

$$0 = \Big(E_e(r_e^2+a^2) - aL_e\Big)^2 - \Delta(r_e^2+K_e), \tag{73}$$

$$0 = K_e - (E_e a - L_e)^2, \tag{74}$$

$$r_e^2\dot{\phi}_e = \frac{1}{\Delta}\Big[2E_eaMr_e + (r_e^2 - 2Mr_e)L_e\Big]. \tag{75}$$

As explained in our previous article, the constants of motion can be calculated, following Chandrasekhar (1983), so that, using

$$u = 1/r_e, \tag{76}$$

and

$$Q_{\pm} = 1 - 3Mu \pm 2a\sqrt{Mu^3}; \tag{77}$$

one then obtains that the values of the energy E_e and angular momentum L_e are given by:

$$E_e = \frac{1}{\sqrt{Q_{\mp}}}\Big(1 - 2Mu \mp a\sqrt{Mu^3}\Big), \tag{78}$$

and

$$L_e = \mp\frac{\sqrt{M}}{\sqrt{uQ_{\mp}}}\Big(a^2u^2 + 1 \pm 2a\sqrt{Mu^3}\Big); \tag{79}$$

where upper sing applies to retrograde orbits while lower sign applies to direct orbits.

The range of validity of the these equations has been discussed in our previous article; we here just note that calling r_c the relevant root of Q, then for $r_+ \leq r < r_c$ we will use the same values of energy and angular momentum, as those for the last stable orbit.

In this respect, let us recall that the unstable circular photon orbit on the equatorial plane is given by

$$r_c = 2M\left(1 + \cos\left(\frac{2}{3}\arccos\left(\pm\frac{a}{M}\right)\right)\right); \tag{80}$$

where upper sing applies to retrograde orbits while lower sign applies to direct orbits.

For the calculation of the flux we need the factor

$$1/(1+z)^4 = 1/(u^b_e\ell_b)^4, \tag{81}$$

where

$$g_{ab}u^a_e\ell^b = E_e\dot{t} - L_e\dot{\phi}. \tag{82}$$

4 SIMULATED IMAGES WITH GRAVITATIONAL LENS MAGNIFICATION AND RED/BLUESHIFT EFFECTS

4.1 Basic model

In this work we use for the mass of the supermassive black hole the value published in Abuter et al. (2022), which is $M = 4.3 \times 10^6 M_{\odot}$

The direction of the angular momentum was deduced from reference Reid & Brunthaler (2020), interpreting the apparent motion of Sgr A*, as due to the motion of the solar system, and its surroundings around the center supermassive black hole. In this way we assign the direction of the angular momentum to be 30.22° south of west direction.

4.2 Image from the EHT Collaboration of Sagittarius A*

In Fig. 1 we reproduce the EHT image of Sagittarius A*, that we use as our main reference for this work. The image is a reconstruction made from observations taken on April 7 of 2017; it consists of the average of another four images, each one of them obtained from a larger set of reconstructions. According to the EHT, these four groups were a convenient way to manage the analysis of the observed differences shown by the several resulting images with the diverse processing pipelines employed. Three of the four clusters were intended to separate ring structures having a salient bright spot at different sectors of the image and the fourth one group intended to detect non-ring morphologies. The relative contribution of each cluster to the final image can be seen in fig. 13 of Akiyama et al. (2022c); in particular, it shows that most of the reconstruction obtained are those having bright spots at north-west and south-west position angle (PA). Then, the results presented exhibit some dependency on the choice of parameter used by the imaging pipelines as well as the imagine procedure itself. The observational challenges related with the imaging process of Sagittarius A* and the remaining degeneracy in the final results leave several open questions. For instance, does it becomes appropriated to consider averages of a set of images in order to picture features of the object under study? Since different reconstruction methods produce different features one could ask which of them are physically representative of the source. A common feature that also appears in most of the reconstructed images is a bright ring, but since the reconstruction algorithm needed additional input, the question still remains if the choices of parameter has been the optimum. Some of these points have been addressed in reference Akiyama et al. (2022c) (see section 7.5) pointing that non-ring structures are very unlikely.

The presence of an elliptical ring structure in the image of EHT, suggests a source which is observed fairly face-on. This has been our first assumption that we study in detail in subsection 4.3: while in subsection 4.4 we will consider another geometry.

Beyond the three brighter regions shown in the image; it is somehow striking the elliptical shape, of the visible background structure, that it could suggest a matter distribution more or less with the shape of an inclined disk. What is striking is that the angle of the semimajor axis, of this structure, is not contained in the plane of the galaxy. Also the bright region on the top of this image, supports this interpretation of an inclined disk.

In any case, for these reasons we have studied the possibility that there were a thin disk with the orientation suggested for this image. This is analysed in the next subsection 4.3. But also, in subsection 4.4 we study the more natural expected situation, that the projected angular momentum of the black holeis aligned with the angular momentum of the galaxy.

4.3 Graphs with angular momentum aligned perpendicularly to the elliptical shape of the EHT image

In this subsection we show the graphs corresponding to images calculated with an angular momentum of the black hole, whose projection coincide with the perpendicular direction to the semi-mayor axis of the elliptical image published by the EHT Collaboration team for Sagittarius A*. We use the following values of iota: $\iota = -0.1745$, $\iota = -0.3490$, $\iota = -0.5235$, $\iota = -0.6980$, $\iota = -0.8725$, $\iota = -1.0470$, $\iota = -1.2215$, $\iota = -1.3960$; corresponding to degrees of -10^o, -20^o, -30^o, -40^o, -50^o, -60^o, -70^o, -80^o, of the angle of the black hole angular momentum with the plane of the image. From left to right, in each figure we show the images corresponding to $a = 0.98$, $a = 0.75$, $a = 0.50$, $a = 0.25$ and $a = 0.00$ respectively.

The comparison of images is very complicated, and it is difficult to have a universal way to be applied to any situation. In our case, we use our understanding of the possible astrophysical situation, but we also use a direct numerical measure employing the correlation coefficient of the comparison of the EHT image with our images. This is not an ideal measure, but it provides a minimum information of coincidence between images. In particular we will see in this set that high values of the correlation coefficient do not necessarily provide good coincidence of the images. We have encounter the same problematic in our previous work (Boero & Moreschi 2021) which can be consulted for further explanation.

In Fig. 10 we present the graph of the correlation coefficient between the EHT image and our images.

It can be seen that the position of the lump, in our images, with the highest intensity does not coincide with none of the three most intense zones, seen in the elliptical EHT image. For this reason in the next subsection we study images where the projection of the angular momentum of the black hole, coincides with the expected direction for the angular momentum of the galaxy.

4.4 Graphs with angular momentum aligned with the angular momentum of the galaxy

The rather high values of the correlation coefficient shown in Fig. 10 is not convincing evidence for us that the synthetic images are giving a good representation of the EHT image. In fact, one can clearly notice that the morphology of them are very different, and this is a quality that is not meassured by the correlation coefficient.

From figure 11 to 20 we show the graphs corresponding to images calculated with an angular momentum of the black hole, whose projection coincide with that of the angular momentum of the galaxy. From left to right, in each figure we show the images corresponding to $a = 0.00$, $a = 0.25$, $a = 0.50$, $a = 0.75$ and $a = 0.98$ respectively.

It should be notice that due to the small inclination of the disc, simulated images require a very good control of numerical errors since magnification effects becomes divergent near the emission disc region.

For convenience we also present the table of the correlations that produce the graphs in this

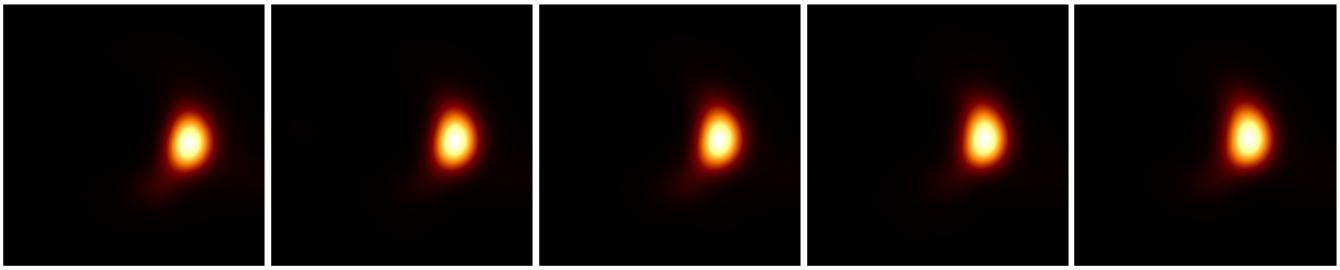

Figure 2. $\iota = -0.1745 = -10°$, and from left to right with Kerr parameter: $a = 0.00$, $a = 0.25$, $a = 0.50$, $a = 0.75$ and $a = 0.98$.

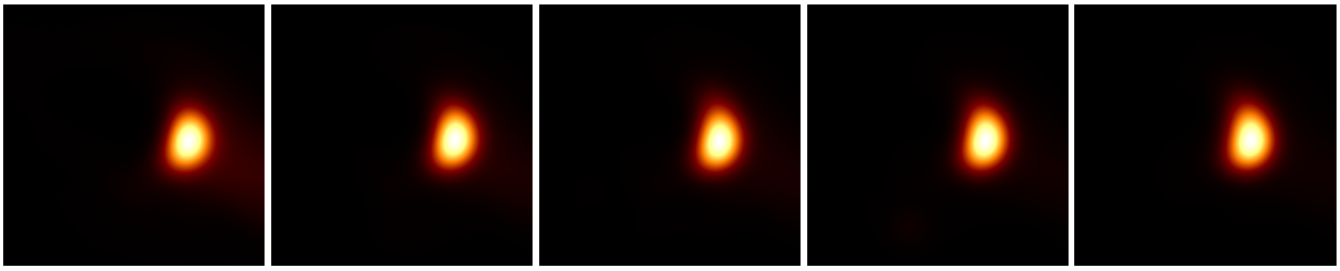

Figure 3. $\iota = -0.3490 = -20°$, and from left to right with Kerr parameter: $a = 0.00$, $a = 0.25$, $a = 0.50$, $a = 0.75$ and $a = 0.98$.

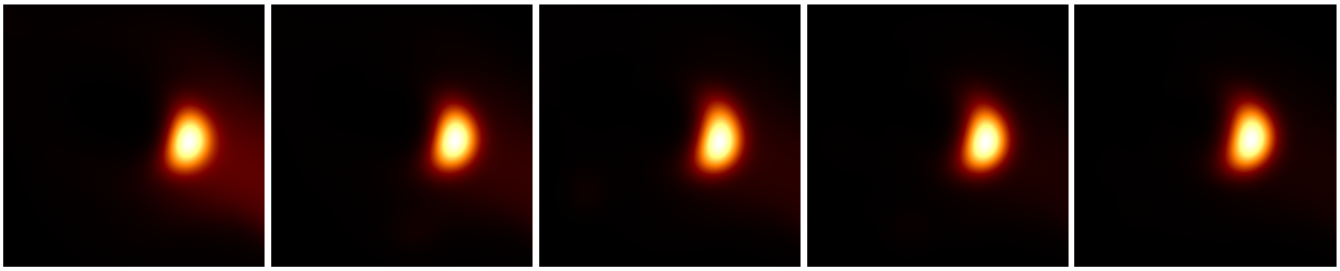

Figure 4. $\iota = -0.5235 = -30°$, and from left to right with Kerr parameter: $a = 0.00$, $a = 0.25$, $a = 0.50$, $a = 0.75$ and $a = 0.98$.

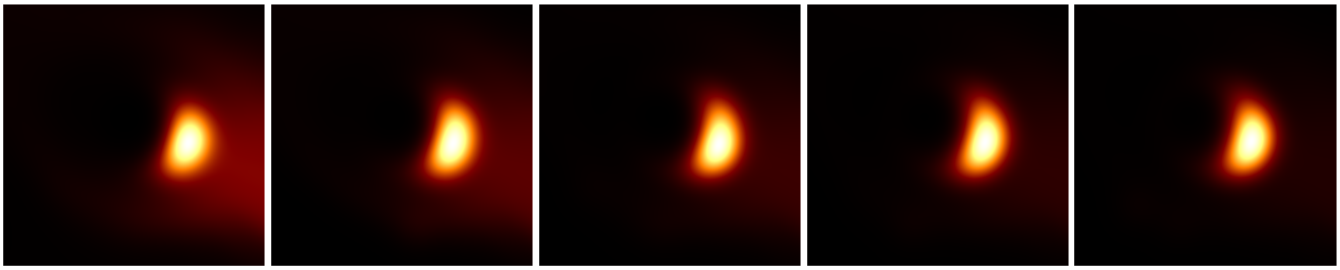

Figure 5. $\iota = -0.6980 = -40°$, and from left to right with Kerr parameter: $a = 0.00$, $a = 0.25$, $a = 0.50$, $a = 0.75$ and $a = 0.98$.

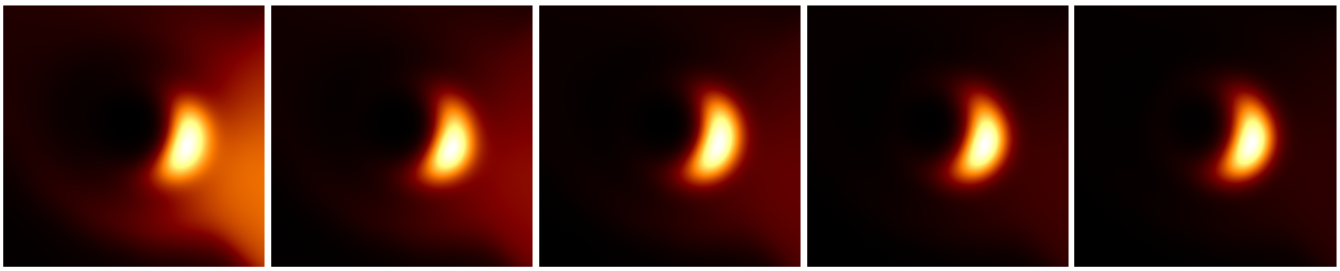

Figure 6. $\iota = -0.8725 = -50°$, and from left to right with Kerr parameter: $a = 0.00$, $a = 0.25$, $a = 0.50$, $a = 0.75$ and $a = 0.98$.

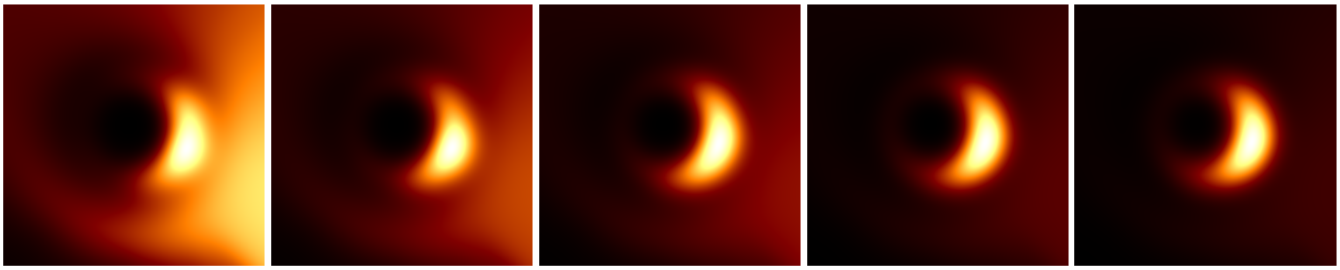

Figure 7. $\iota = -1.0470 = -60°$, and from left to right with Kerr parameter: $a = 0.00$, $a = 0.25$, $a = 0.50$, $a = 0.75$ and $a = 0.98$.

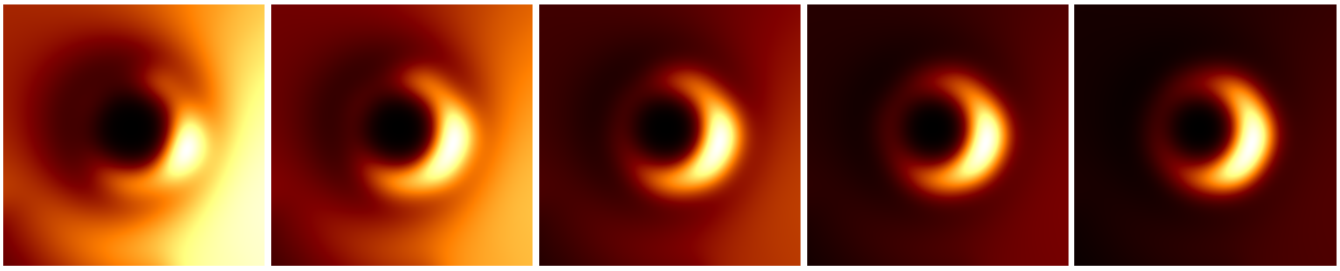

Figure 8. $\iota = -1.2215 = -70°$, and from left to right with Kerr parameter: $a = 0.00$, $a = 0.25$, $a = 0.50$, $a = 0.75$ and $a = 0.98$.

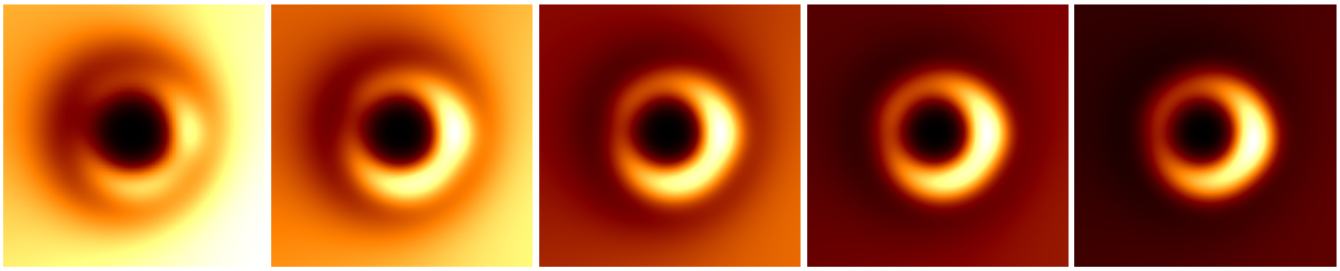

Figure 9. $\iota = -1.3960 = -80°$, and from left to right with Kerr parameter: $a = 0.00$, $a = 0.25$, $a = 0.50$, $a = 0.75$ and $a = 0.98$.

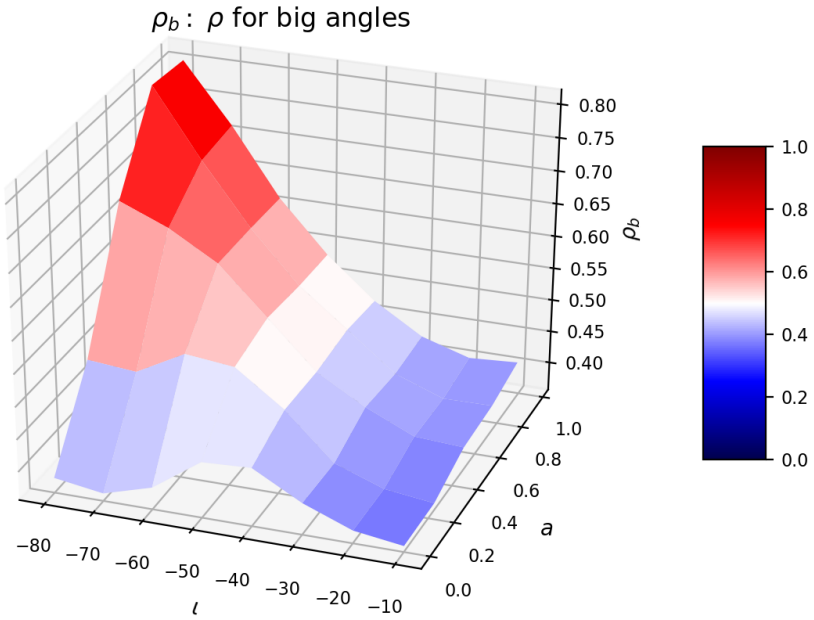

Figure 10. Comparison of the above graphs, with big angles, against the EHT image, through the calculation of the correlation, as explained in the text.

Figure 11. $\iota = -0.0873 = -5°$, and from left to right with Kerr parameter: $a = 0.00$, $a = 0.25$, $a = 0.50$, $a = 0.75$ and $a = 0.98$.

Figure 12. $\iota = -0.0300 = -1.72°$, and from left to right with Kerr parameter: $a = 0.00$, $a = 0.25$, $a = 0.50$, $a = 0.75$ and $a = 0.98$.

Figure 13. $\iota = -0.0030 = -0.172°$, and from left to right with Kerr parameter: $a = 0.00$, $a = 0.25$, $a = 0.50$, $a = 0.75$ and $a = 0.98$.

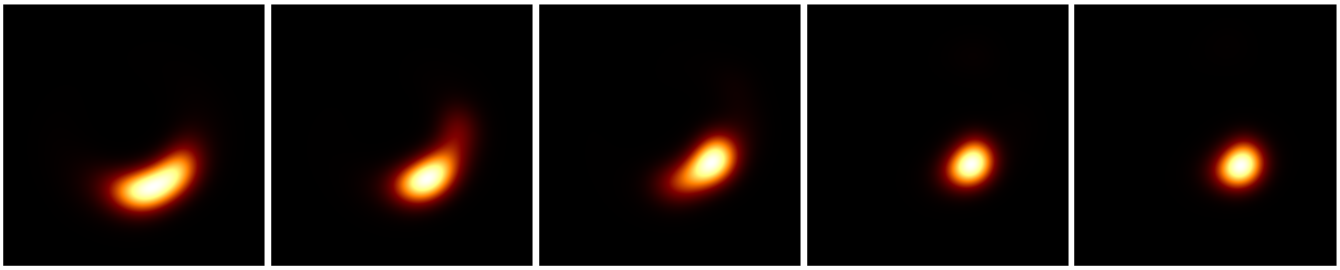

Figure 14. $\iota = -0.0003 = -0.0172°$, and from left to right with Kerr parameter: $a = 0.00$, $a = 0.25$, $a = 0.50$, $a = 0.75$ and $a = 0.98$.

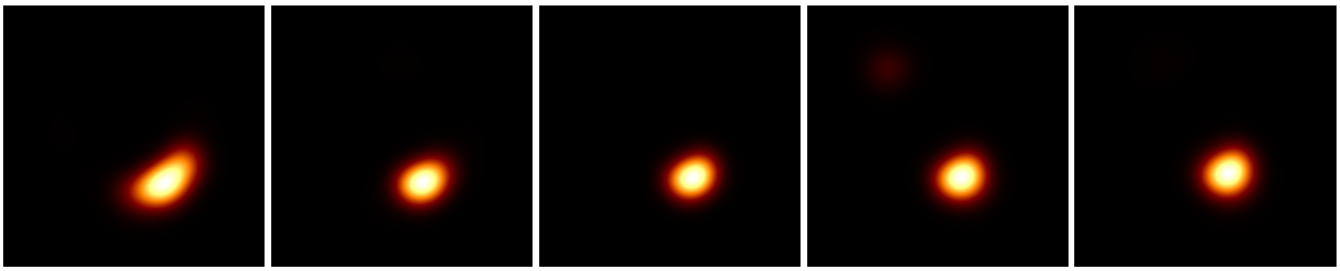

Figure 15. $\iota = -10^{-6} = -0.00005729°$, and from left to right with Kerr parameter: $a = 0.00$, $a = 0.25$, $a = 0.50$, $a = 0.75$ and $a = 0.98$.

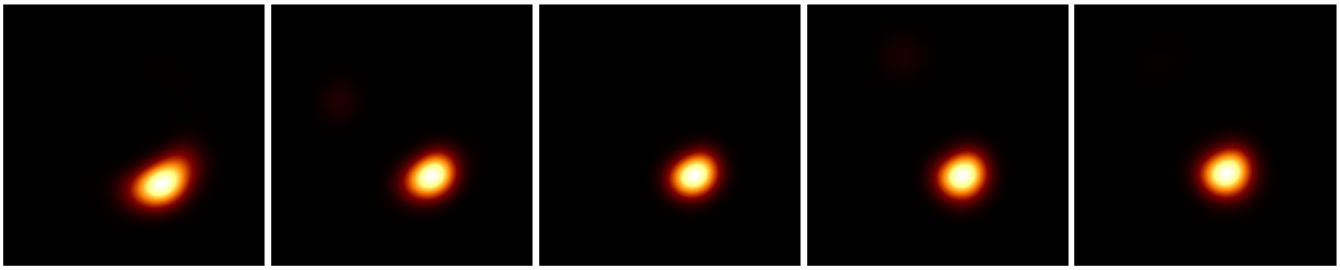

Figure 16. $\iota = 10^{-6} = 0.00005729°$, and from left to right with Kerr parameter: $a = 0.00$, $a = 0.25$, $a = 0.50$, $a = 0.75$ and $a = 0.98$.

Figure 17. $\iota = 0.0003 = 0.0172°$, and from left to right with Kerr parameter: $a = 0.00$, $a = 0.25$, $a = 0.50$, $a = 0.75$ and $a = 0.98$.

Figure 18. $\iota = 0.0030 = 0.172°$, and from left to right with Kerr parameter: $a = 0.00$, $a = 0.25$, $a = 0.50$, $a = 0.75$ and $a = 0.98$.

Figure 19. $\iota = 0.0300 = 1.72°$, and from left to right with Kerr parameter: $a = 0.00$, $a = 0.25$, $a = 0.50$, $a = 0.75$ and $a = 0.98$.

Figure 20. $\iota = 0.0873 = 5°$, and from left to right with Kerr parameter: $a = 0.00$, $a = 0.25$, $a = 0.50$, $a = 0.75$ and $a = 0.98$.

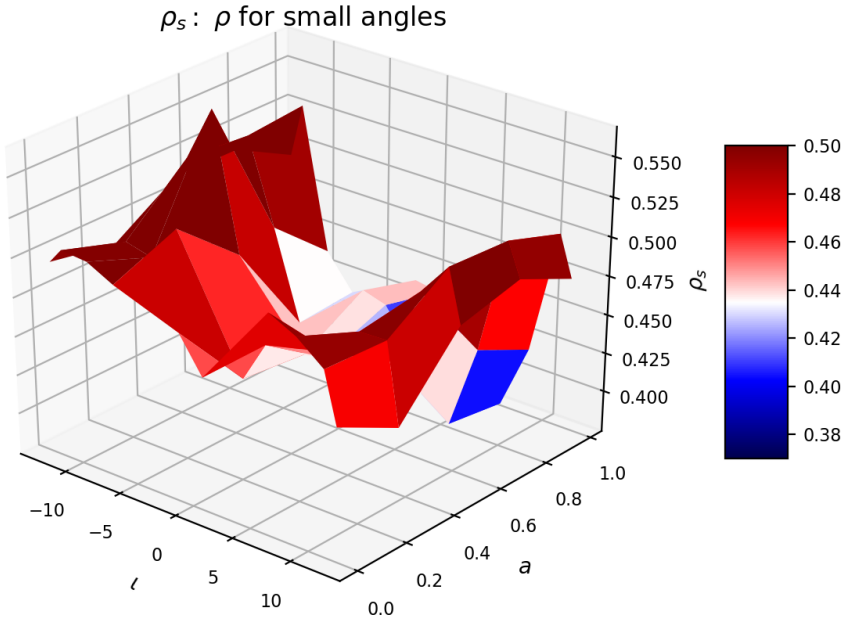

Figure 21. Comparison of the above graphs, with small angles, against the EHT image, through the calculation of the correlation, as explained in the text. The ι axis has the logarithmic scale defined by $\ln(\iota e 10^6)$, where e is Euler number; so that the small angles are magnified.

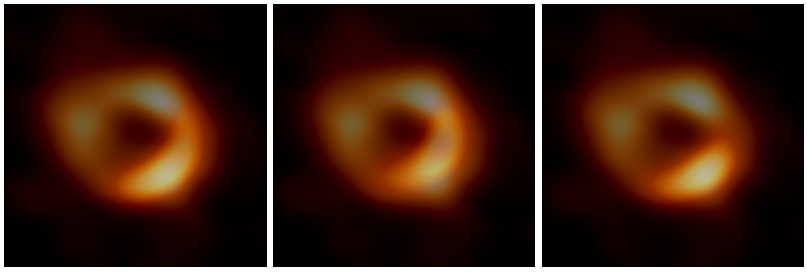

Figure 22. Superposition of best candidates with the original image. These are from left to right, the cases: $a = 0.50$ with $\iota = -0.003$, $a = 0.98$ with $\iota = -0.030$ and $a = 0.50$ with $\iota = -0.030$. It can be seen that the first case shows the best match of the local maximum at the lower right of the image.

0.4969	0.4891	0.5144	0.5140	0.4946
0.5069	0.4937	0.5289	0.5256	0.5290
0.5054	0.4894	0.5646	0.4715	0.4388
0.4968	0.5131	0.4779	0.4143	0.4169
0.4816	0.4324	0.4279	0.4505	0.4395
0.4589	0.4593	0.4312	0.4460	0.4368
0.5142	0.4698	0.4438	0.3825	0.3771
0.5057	0.4889	0.4944	0.4375	0.4194
0.4919	0.4896	0.5156	0.5130	0.5003
0.4590	0.4376	0.4818	0.4915	0.4743

Table 1. Table of values of the correlation for small angles, as shown in Fig. 21.

4.5 End point of null geodesics in Kerr-Schild coordinates

We have presented two sets of simulated images using as a physical model that of a thin disk with different equatorial inclinations with respect to the line of sight, and also for various values of the angular momentum parameter a. For reasons that are being discussed, we take as our best model, the one characterized by the values $a = 0.5$ and $\iota = -0.003$. But the question we would like to tackle now, is, where do all these ray tracing calculation reach, in the vicinity of the black hole? The question is relevant to understand the nature of the image one is generating. The first thing to clarify is the choice of a coordinate system to use, in order to make graphs that have some geometrical meaning that is not corrupted by a bad behavior of the coordinate system; as is known to happen with the Boyer-Lindquist coordinates in the vicinity of the event horizon. Our choice is the Kerr-Schild coordinate system, that is naturally defined when one makes the corresponding decomposition of the Kerr metric, in the so called Kerr-Schild form. In this way we have at our disposal a set of coordinates (t, x, y, z) that we use for these graphs.

In the graphs of Fig. 23 we present the end points of the integration in three different planes. In the top-left graph, it is impressive to see that those trajectories that reach the disk, are almost aligned along the line in the equatorial plane, that is opposite to the line of sight. That is, one has to have in mind the [illegible]

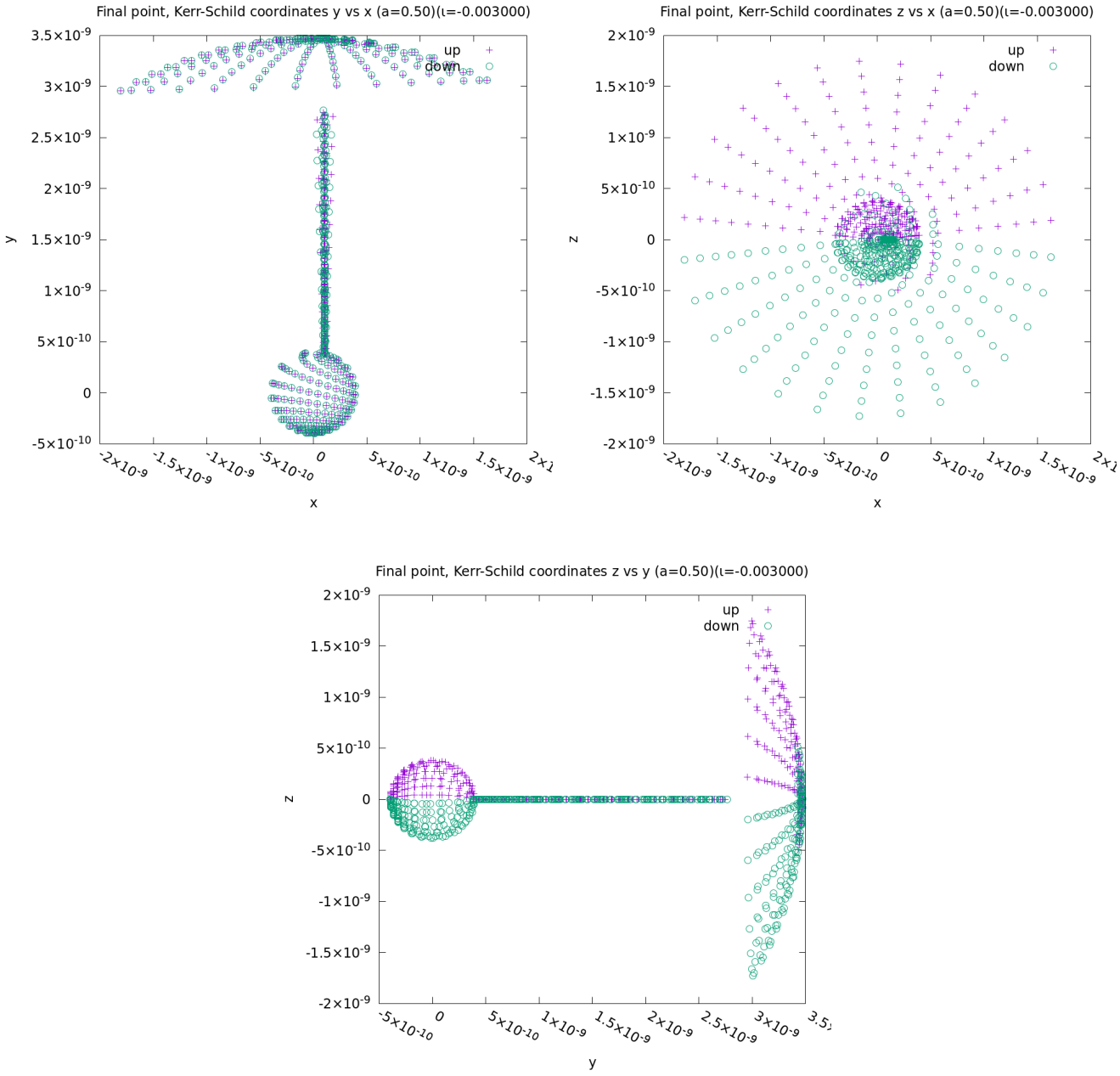

Figure 23. The Kerr-Schild coordinates are adapted to the geometry of the black hole, so that the equatorial plane is $z = 0$, and the angular momentum of the black hole points in the direction of the positive z's. The top-left graph, using (x, y) coordinates, shows the end points of the ray-tracing to the past, for all values of z; where positive y means the zone away from the observer, that is, in the opposite side of the black hole. The top-right graph, using (x, z) coordinates, shows the end points of the null geodesics to the past, for all values of y, the bottom graph, using (y, z) coordinates, shows the end points of the ray-tracing to the past, in this plane for all values of x.

cated somewhere far away with big values of the negative y coordinate. In other words, with these geometrical settings, the observer only sees a very small portion of the disk which is just opposite to the line of sight; since for this small angle, the front part is almost invisible; in fact, non of our geodesics reach any other region of the disk. This is in spite of the fact that we have made the calculation for 1008 geodesics in the plane of the expected image. The upper part of this graph, shows an umbrella type shape, which just shows our choice for the end condition, for those geodesic that have not reached the disk. In the bottom part of the same graph, one can see an sphere like object, which is just the condition that the geodesics have reached the event horizon. For this rather low angular momentum, one can only see a peculiar spread of the end points; where in the whole graph, crosses indicates geodesics that start above the equatorial plane and circles denote geodesics that start below the equatorial plane. The fact that the spread in the disk is so small, also indicates the

degree of precision of our calculations. In particular we have been using quadruple precision with 2.4×10^{-22} tolerance for the Runge-Kutta integrator.

In the top-right graph, showing the (x, z) values, one can see the umbrella type shape, from another angle. A big number of end points, at the opposite side of the black hole, are difficult to see in this graph, since they are confused with the end points of null geodesics that reach the event horizon, and form the sphere like shape object, more or less in the center of this graph.

Finally in the bottom graph of Fig. 23, one can see the same distribution from a different angle; in this case the (x, z) coordinates. Since the equatorial plane coincides with $z = 0$, one can see that the condition for the null geodesics to reach the disk is satisfied with very high precision; which are all those points outside the event horizon with $z = 0$. The umbrella type shape is now shown to the right of this graph.

4.6 The possible bar structure on the disk

In our previous article on the construction of synthetic images of M87(Boero & Moreschi 2021), we recurred to a bar structure on the disk in order to build images that resemble in a better way the corresponding EHT image of the supermassive black hole. For this reason, we have also study for this case of Sgr A*, the consequences of introducing this type of structure. The results did not help in providing better images, that where closer to the aspects found in the EHT image of Sgr A*. And the reason for this, can be understood in terms of the graphs of Fig. 23, discussed previously. That is, since for this geometric configuration, the only observed part of the disk lies on a narrow sector, on the disk, at the opposite region of the line of sight; the introduction of a bar structure with higher temperature, can only be seen if it is placed on this narrow region. And therefore its effect is to slightly change the original image, without bar structure. Consequently we have not included those graphs in this article, since they do not contribute to the search for the explanation of the other structure shown in the EHT image of Fig. 1.

4.7 Numerical comparison of the images

The main part of the construction process of the images, is the analysis of the general aspects of EHT image. Guided by the suggested geometry of Fig. 1, we have made a couple of configuration for our disk model, in order to try to construct images that resemble that of the EHT team. But it is convenient to also have at hand some numerical measure for the comparison of our images with that of EHT. For this reason, as we did in our previous work, we have also considered the correlation between two images. This is a very limited type of measure, that does not include information on the structure of each image; but in any case it is a very natural type of measure.

The comparison of our first configuration, with big angles between the equatorial plane of the disk and the plane of the galaxy are shown graphically in Fig. 10. While, the comparison of our second configuration, with small angles between the equatorial plane of the disk and the plane of the galaxy are shown graphically in Fig. 21. The corresponding table for this last graph is presented in table 4.4; where one can see that our chosen configuration of $a = 0.5$ and $\iota = -0.003$, has the highest value.

5 PHOTON REGIONS AND SILHOUETTE OF THE BLACK HOLE

In a spherically symmetric spacetime it is natural to study the null geodesics that have constant radial coordinate; and so define the corresponding photon region. Surprisingly, in Kerr spacetime, the analog question also has meaning. It should be noticed that since the spacetime is not spherically symmetric, it is not trivial to ask whether there exists a natural radial coordinate; but Kerr's radial coordinateKerr (1963) r seems to be the answer. In fact, there exist null geodesics with r =constant, and they have been called also the generators of the 'photon regions'. However only recently there have been claimsCederbaum & Jahns (2019) that this set contains the only trajectories of photons that do not go cross the horizon or escape to infinity. In relation to all this, it is probably worthwhile to point out that the radial and angular coordinates (r, θ) used in the Boyer-LindquistBoyer & Lindquist (1967) form of the metric, coincide with the original (r, θ) presented in Kerr's article.

Although the photon regions have been studied in several works, we are only concerned here with the silhouette that an observer would see of a black hole with angular momentum, if seen with a lighted background.

Then, we are concerned with the null geodesics that satisfy $r = r_p$, and so, $\dot{r} = 0$ and $\ddot{r} = 0$; or equivalently, $\mathcal{R} = 0$ and $\frac{d\mathcal{R}}{dr} = 0$, which can be expressed as:

$$0 = \left(E\left(r_p^2 + a^2\right) - aL\right)^2 - K\Delta(r_p),, \tag{83}$$

and

$$0 = 2Er_p\Big(E\left(r_p^2 + a^2\right) - aL\Big) - K(r_p - m). \tag{84}$$

From these one obtains

$$\frac{\Delta(r_p)}{(r_p - m)} = \frac{\left(E\left(r_p^2 + a^2\right) - aL\right)}{2Er_p}; \tag{85}$$

where we have divided the above equations. Note that E is of order one and negative, while $|aL| << |Er_p^2|$; implying that the $\left(E\left(r_p^2 + a^2\right) - aL\right)$ is negative, so that (85) has the correct sign. Then, one has

$$L = \frac{1}{a}\Big(E\left(r_p^2 + a^2\right) - \frac{2Er_p\Delta(r_p)}{(r_p - m)}\Big); \tag{86}$$

and

$$K = \frac{(2Er_p)^2\Delta(r_p)}{(r_p - m)^2}. \tag{87}$$

One also must satisfy

$$K - \left(\frac{L}{\sin(\theta_p)} - aE\sin(\theta_p)\right)^2 \geqslant 0. \tag{88}$$

Then, (86) gives $L(r_p)$, while (87) gives $K(r_p)$. To obtain the silhouette [illegible]

touch the outer boundary of this regions, which is characterized by the condition that $\dot{\theta_p} = 0$ or equivalently

$$K(r_p) - \left(\frac{L(r_p)}{\sin(\theta_p)} - aE\sin(\theta_p)\right)^2 = 0. \tag{89}$$

This allows to express $r_p(\theta_p)$, since one has

$$\frac{(2Er_p\sin(\theta_p))^2\Delta(r_p)}{(r_p-m)^2} = \left(L(r_p) - aE\sin(\theta_p)^2\right)^2, \tag{90}$$

or

$$\Delta(r_p)\frac{(2Er_p\sin(\theta_p))^2}{(r_p-m)^2} = \left(\frac{1}{a}\left(E\left(r_p^2+a^2\right) - \frac{2Er_p\Delta(r_p)}{(r_p-m)}\right) - aE\sin(\theta_p)^2\right)^2, \tag{91}$$

so that

$$\begin{aligned}\Delta(r_p)\frac{(2ar_p\sin(\theta_p))^2}{(r_p-m)^2} = \\ \left(r_p^2+a^2 - \frac{2r_p\Delta(r_p)}{(r_p-m)} - a^2\sin(\theta_p)^2\right)^2 = \\ \left(r_p^2+a^2\cos(\theta_p)^2 - \frac{2r_p\Delta(r_p)}{(r_p-m)}\right)^2.\end{aligned} \tag{92}$$

Taking the square root one would have a $\pm$ relation, but we can build this in the definition of ϑ_p with a range of $[-\pi,\pi]$; so that we can write

$$\begin{aligned}\sqrt{\Delta(r_p)}2ar_p\sin(\vartheta_p) = \\ (r_p-m)\left(r_p^2+a^2\cos(\vartheta_p)^2\right) - 2r_p\Delta(r_p);\end{aligned} \tag{93}$$

which provides for us $r_p(\vartheta_p)$. Defining $f(r_p)$ as

$$\begin{aligned}f(r_p) =&(r_p-m)\left(r_p^2+a^2\cos(\vartheta_p)^2\right) - 2r_p\Delta(r_p) \\ &- \sqrt{\Delta(r_p)}2ar_p\sin(\vartheta_p);\end{aligned} \tag{94}$$

one could solve for r_p using the standard techniques of root finding.

Then we obtain $L(\vartheta_p)$ and $K(\vartheta_p)$; from which we draw the silhouette using celestial coordinates.

Note that when $a = 0$ one has

$$\begin{aligned}f(r_p) =&(r_p-m)r_p^2 - 2r_p\Delta(r_p) \\ =&r_p^3 - mr_p^2 - 2r_p(r_p^2-2mr_p) \\ =&-r_p^3+3mr_p^2;\end{aligned} \tag{95}$$

so that $r_p = 3m$ in this case.

6 FINAL COMMENTS

As commented previously, the EHT collaboration has used as guiding idea, the structure of rings for the construction of their images. The question of whether Sgr A* is appropriately described by a ring, is so central to the EHT work(Akiyama et al. 2022c) that they dedicate a subsection to this point. They affirm there that: "there are a small number of non-ring images that fit the data well and cannot easily be excluded through additional tests."

In our work we have applied as guiding idea the structure of a disk, which was very successful in the construction of images for the M87 system. Since they also consider the with of the rings, one may wonder whether there could be some kind of intersection between the two main ideas of the models. We can point out, that since the main starting physical model are rather different, also the language is different; but it should be remarked that they concentrate on rings that are mostly face-on, in contrast to our assumption of inclined thin accretion disks, that are mostly edge-on.

The main EHT image shown in Fig. 1 shows a basic structure of three local intensity maxima located approximately at position angles of: (A: 70°), (B: 220°) and (C: 330°); on a disk like shape. Interpreting this configuration as a possible disk, which was inclined to the observer, and assuming that structure C indicated the opposite side of the disk, we first carried out a series of images, for the iota angle in the range $\iota \in [-10°, -80°]$, and with the angular parameter a with values $a = [0, 0.25, 0.50, 0.75, 0.98]$. We conclude that the images so constructed do not represent consistently the EHT image of Sgr A*. For this reason we next performed calculation of images that assume the more natural configuration of a disk, with small angle variations with respect of the plane of the galaxy. In all cases we have assumed the disk is located in the equatorial plane of the black hole, and therefore, its angular momentum is perpendicular to the disk. With this second set of images, we find that one can explain the structure B of the EHT image. The model we have used does not account for the other structures A and C of the EHT image.

It should be remembered that the final EHT image is the average of four different images that they show in their Figure 13 graphs. However it is noticed that only structure B is persistent in the four basic images; probably indicating that it is a stable physical structure observed by the EHT team.

This fact is reinforced if we take a look at the first row in Figure 27 of the EHT article Akiyama et al. (2022d) which we reproduce here in Fig. 25. The important graphs, that we reproduce in Fig. 25 are the first and the third; where they show the images that are obtained from the THEMES image algorithm. In their paper III, in which they present the preferred image of Sgr A*, they have chosen to use the data of April 7. However, it is noticeable that the THEMES image from April 6, shows a prominent local intensity maximum more or less at the position of the local intensity maximum or our preferred image shown in Fig. 24. This gives support to our conjecture that structure B corresponds to an intrinsic persistent structure of Sgr A*.

As it has been mentioned in the EHT articles, the acquisition of the data and its processing is a very difficult task that forces the team to use models, with different weights, in the reconstruction of images. We hope our work can contribute to the adjustments of pipelines that are used in those reconstructions processes; since different priors produce various outcomes.

Data Availability

No new data were generated or analysed in support of this research. The numerical calculation is completely described in the article. IF-2023-00750886-UNC-ME#FAMAF

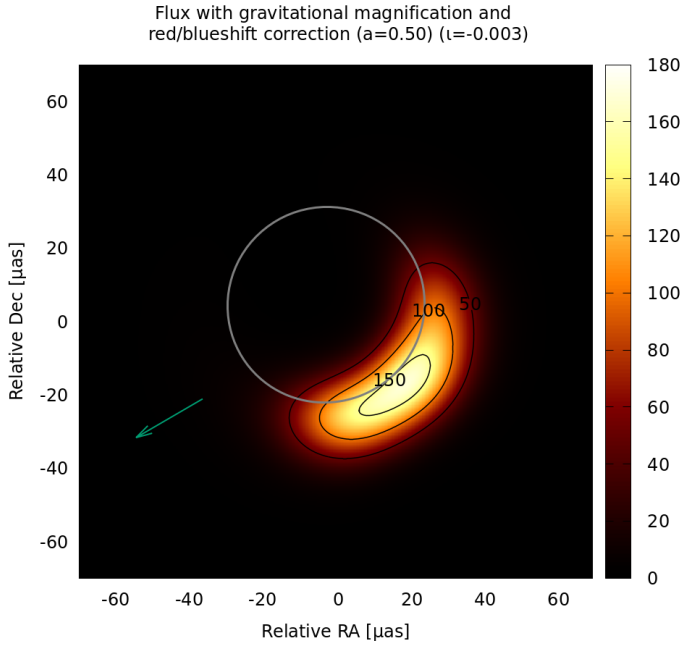

Figure 24. Image of the flux with all magnifications for Sagittarius A* in the case of $a = 0.50$ and $\iota = -0.003$; where the grey line shows the silhouette for the case of a back illumination of the supermassive black hole.

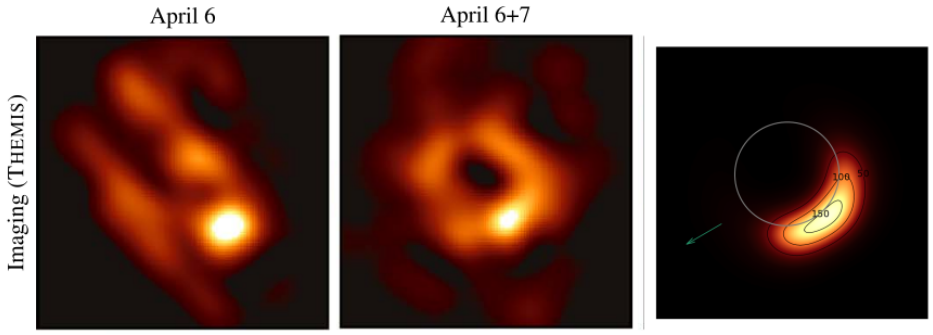

Figure 25. Reproduction of two graphs first row of Figure 27 of paper IV of the EHT work on Sgr A*; they correspond to April 6 and April 6+7 of the Themis pipeline. The third graph on the right is the copy of our image at the scale of the other EHT images.

Acknowledgments

We acknowledge support from CONICET, SeCyT-UNC and Foncyt.

REFERENCES

Abuter R., et al., 2022, Astron. Astrophys., 657, L12
Akiyama K., et al., 2019a, Astrophys. J., 875, L1
Akiyama K., et al., 2019b, Astrophys. J., 875, L4
Akiyama K., et al., 2022a, Astrophys. J. Lett., 930, L12
Akiyama K., et al., 2022b, Astrophys. J. Lett., 930, L13
Akiyama K., et al., 2022c, Astrophys. J. Lett., 930, L14
Akiyama K., et al., 2022d, Astrophys. J. Lett., 930, L15
Akiyama K., et al., 2022e, Astrophys. J. Lett., 930, L16
Akiyama K., et al., 2022f, Astrophys. J. Lett., 930, L17
Boero E. F., Moreschi O. M., 2020, Mon. Not. Roy. Astron. Soc., 492, 3763
Boero E. F., Moreschi O. M., 2021, Mon. Not. Roy. Astron. Soc., 507, 5974
Boyer R. H., Lindquist R. W., 1967, J.Math.Phys., 8, 265
Carter B., 1966, Phys. Rev., 141, 1242
Cederbaum C., Jahns S., 2019, Gen. Rel. Grav., 51, 79
Chandrasekhar S., 1983, The mathematical theory of black holes. Oxford University Press, 646 p.
Ichimaru S., 1977, Astrophys. J., 214, 840
Kerr R. P., 1963, PRL, 11, 237
Reid M. J., Brunthaler A., 2020, Astrophys. J., 892, 7
Shapiro S. L., Lightman A. P., Eardley D. M., 1976, Astrophys. J., 204, 187
Yuan F., Narayan R., 2014, Ann. Rev. Astron. Astrophys., 52, 529

This paper has been typeset from a TEX/LATEX file prepared by the author.

IF-2023-00750886-UNC-ME#FAMAF

Universidad Nacional de Córdoba
1983/2023 - 40 AÑOS DE DEMOCRACIA

Hoja Adicional de Firmas
Informe Gráfico

Número: IF-2023-00750886-UNC-ME#FAMAF

CORDOBA, CORDOBA
Viernes 1 de Septiembre de 2023

Referencia: MORESCHI- Documentacion informe año sabatico parte 5//
EX-2021-00478970- -UNC-ME#FAMAF

El documento fue importado por el sistema GEDO con un total de 15 pagina/s.

Digitally signed by GDE UNC
DN: cn=GDE UNC, c=AR, o=Universidad Nacional de Cordoba, ou=Informatica, serialNumber=CUIT 30546670623
Date: 2023.09.01 12:30:39 -03'00'

SILVIA ANAHI VERON
Administrativa
Mesa de Entradas Facultad de Matemática, Astronomía, Física y Computación
Universidad Nacional de Córdoba

Digitally signed by GDE UNC
DN: cn=GDE UNC, c=AR, o=Universidad Nacional de Cordoba, ou=Informatica, serialNumber=CUIT 30546670623
Date: 2023.09.01 12:30:45 -03'00'